Steel and Composite Structures, *Vol. 27, No. 3 (2018) 337-353*
DOI: https://doi.org/10.12989/scs.2018.27.3.337

Cyclic performance and design recommendations of a novel weak-axis reduced beam section connection

Linfeng Lu [*1], Yinglu Xu [1a], Jie Liu [1b] and James B.P. Lim [2c]

[1] *School of civil engineering, Chang'an University, 75 Chang'an Middle Rd, Xi'an, PR China*
[2] *Department of Civil and Environmental Engineering, University of Auckland (City Campus), Engineering Building, 20 Symonds Street, Auckland, New Zealand*

(*Received December 9, 2017, Revised March 12, 2018, Accepted March 15, 2018*)

Abstract. In previous weak-axis moment connection tests, brittle fracture always initiated near the edge of the beam flange groove weld due to force flow towards the stiffer column flanges, which is the opposite pattern as strong-axis moment connections. As part of the China NSFC (51278061) study, this paper tested two full-scale novel weak-axis reduced beam section moment connections, including one exterior frame connection specimen SJ-1 under beam end monotonic loading and one interior frame joint specimen SJ-2 under column top cyclic loading. Test results showed that these two specimens were able to satisfy the demands of FEMA-267 (1995) or ANSI/AISC 341-10 (2010) without experiencing brittle fracture. A parametric analysis using the finite element software ABAQUS was carried out to better understand the cyclic performance of the novel weak-axis reduced beam section moment connections, and the influence of the distance between skin plate and reduced beam section, *a*, the length of the reduced beam section, *b*, and the cutting depth of the reduced beam section, *c*, on the cyclic performance was analyzed. It was found that increasing three parametric values reasonably is beneficial to forming beam plastic hinges, and increasing the parameter *a* is conducive to reducing stress concentration of beam flange groove welds while increasing the parameters *b* and *c* can only reduce the peak stress of beam flange groove welds. The rules recommended by FEMA350 (2000) are suitable for designing the proposed weak-axis RBS moment connection, and a proven calculation formulation is given to determine the thickness of skin plate, the key components in the proposed weak-axis connections. Based on the experimental and numerical results, a design procedure for the proposed weak-axis RBS moment connections was developed.

Keywords: steel frame; weak-axis connection; bending connection; panel zone; I-section column; H-shaped beam

1. Introduction

During the 1994 Northridge and 1995 Kobe earthquakes, extensive full-weld connections and welded flange-bolted web connections suffered unexpected brittle fractures. Since then the prescriptive "pre-Northridge" moment connections have been removed from the Uniform Building Code (1994) and extensive work has been conducted to find methods to improve the seismic performance of steel moment connections.

Although there are many new types of connections (Rezaifar and Younesi 2016, Zahrai *et al*. 2017a, b), the traditional reduced beam section (RBS) connection is still widely used now, which involves the removal of a portion of the beam flanges a short distance from the column face. In this way, the plastic hinge could be moved away from the column-to-beam connections, allowing stable yielding of the beam in the RBS region. From 1996 (Chen *et al*. 1996), the RBS connections have demonstrated successful behavior in numerous laboratory tests involving strong-axis moment connections (Lignos *et al*. 2010, Crisan and Dubina 2016). However, when the RBS beam is framed into the weak-axis of the column, information on cyclic behavior is very limited compared to strong-axis moment connection.

Gilton and Uang (2002) conducted an experimental study for two full-scale weak-axis RBS moment connections, and it was found that both specimens were able to reach the required 0.03 rad of plastic rotation without experiencing a brittle fracture or large stress concentrations at the critical section. A design procedure for weak-axis RBS moment connections was developed then. Oh *et al*. (2015) evaluated the seismic behavior of weak axis column-tree connections, and results showed that two specimens with the RBS and tapered beam section successfully developed ductile behavior without brittle fracture until 5% story drift ratio. Lee *et al*. (2015) designed test specimens according to the procedure proposed by Gilton and Uang (2002), but a simplified sizing procedure for attaching the beam web to the shear plate in the form of C-shaped fillet weld was used. The test results showed that the sharp corner of C-shaped fillet weld tended to be the origin of crack propagation due to stress concentration; because of the presence of weld access hole, a kind of CJP

*Corresponding author, Ph.D., Professor,
E-mail: lulinfeng@chd.edu.cn
[a] Ph.D. Student, E-mail: 2015028003@chd.edu.cn
[b] Ph.D., Associate Professor,
E-mail: james.lim@auckland.ac.nz

ISSN: 1229-9367 (Print), 1598-6233 (Online)

(a) Strong-axis (b) Weak-axis

Fig. 1 Stress profile across beam flange welds

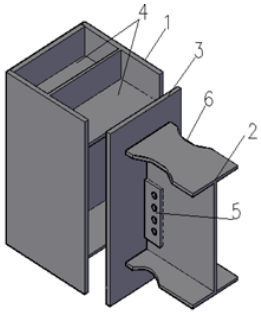

1- I-section column
2- H-shaped beam
3- Skin plate
4- Diaphragm
5- Shear plate
6- Reduced beam flange

Fig. 2 Novel Weak-axis RBS connection

butt joint formed between the beam flange and the horizontal continuity plate in weak-axis moment connections.

For the moment connections of I-section column to H-shape beam, FEMA-355D (2000) proved that the stress profile across beam flange in strong-axis direction is different from the weak-axis connection, as shown in Fig. 1. There were large stress concentrations due to force flow towards the stiffer column flanges in weak-axis connection, which is the opposite pattern as strong-axis moment connections. In fact, as early as 1982, Driscoll and Beddle (1982) reported that the tri-axial tension stresses were present along the continuity plate due to restraint provided by the beam flange groove weld and they reach a maximum at the edge of the beam flange groove weld, and the strain concentration pattern of weak-axis moment connections makes them highly susceptible to brittle fracture of the beam flange groove weld.

Lu *et al*. (2016, 2017) reported two series of tests on weak axis moment connections, which involved a novel weak-axis RBS moment connection (Fig. 2), and confirmed that this type of connection exhibited satisfactory levels of plastic rotation ability. The maximum plastic rotation angle of frame exterior joint specimen under beam-end monotonic loading was greater than 0.03 rad, thus satisfied the requirements of FEMA-267 (1995), one of the current general and recognized evaluation standard in the world. Furthermore, under column top cyclic loading, the frame interior joint specimen showed good hysteretic performance, and satisfied the requirements of ANSI/AISC 341-10 (2010) that beam-to-column connections used in special moment frames (SMF) shall be capable of accommodating flexural resistance of at least 0.80 M_p at the story drift angle of 0.04 rad. Other numerical analysis researches done by Xu *et al*. (2016) pointed this type of connection had good cyclic behavior close to the box-column connection.

Based on the experimental researches done by Lu *et al*. (2016, 2017), this paper will introduce some key technical test data that had never been reported, and conduct parametric analysis using numerical methods for the proposed weak-axis RBS connection to summarize critical factors and develop the design procedure for this connection. In this paper, it needs to point that the geometric unit is millimeter if a geometric dimension has no unit mark, and some notation calculation method, such as joint moment (M), joint rotation angle (θ), joint plastic rotation angle (θ_p), ductility coefficient and other notations shown in the following figures and tables, can be referred to Lu *et al*. (2018).

(a)Specimen installation

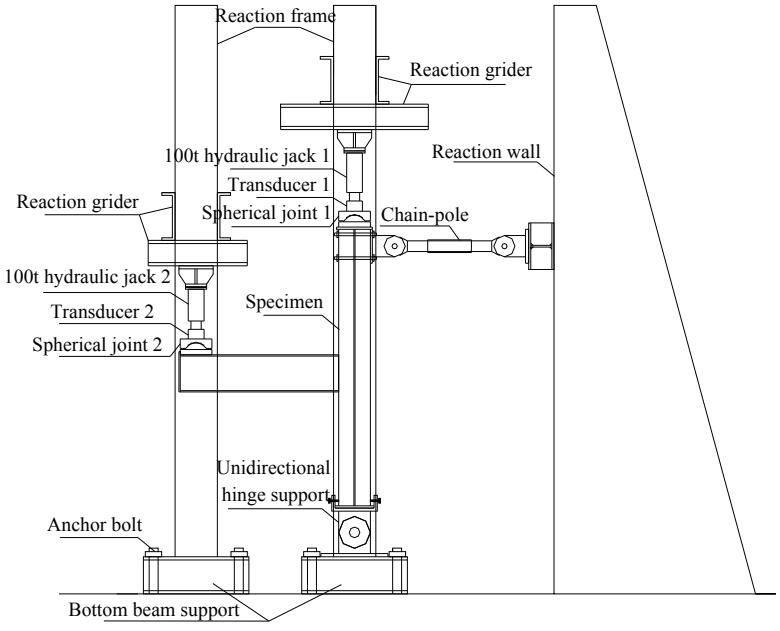

(b) Testing apparatus diagram

Fig. 3 Test setup of specimen SJ-1

2. Experimental and numerical analysis on frame joint specimen SJ-1

2.1 Experimental analysis of exterior joint specimen SJ-1 under beam end monotonic loading

In order to investigate the mechanical behavior of the proposed weak-axis RBS connection details, an exterior frame joint specimen SJ-1 was firstly constructed under the assumption that the bending moment inflection points are close to the middle point of column and beam respectively in a frame. Fig. 3 shows the test setup of specimen SJ-1, and Fig. 4 presents the connection details of specimen SJ-1. The load was applied vertically at the beam end, with the top and bottom of the column being pin connections, and a vertical hydraulic jack was used to apply an axial compression ratio of 0.3 on the top of the column to simulate the effect of the upper floors in a multistory building. I-section Q235B steel column with dimensions of HW300×300×10×15 (height: 3,000 mm, calculated from the upper hinge point to the lower hinge point) and H-shaped Q235B steel beams with dimensions of HN 350×175×7×11 (span: 1,500 mm) were used; the steel plates, too, were made of Q235 steel with nominal yield strength of 235 MPa. In detail, the shear plate and the diaphragms of the column were 12 mm thickness, and the skin plates used were 16 mm thickness.

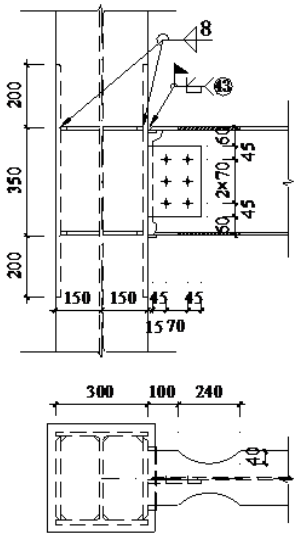

Fig. 4 Connection details of specimen SJ-1

Fig. 5(a) provides the failure mode of specimen SJ-1 after the loading procedure. It can be seen that the plastic hinge moved away from the skin plate face, and the RBS region developed an extensive inelastic deformation, with the beam-column connection region being in good condition without any welds cracking.

To investigate the stress distribution of beam flange groove welds, seven strain gauges were attached close enough to the beam top flange groove welds, named I-I section, and another five strain gauges were placed in the RBS center of beam top flange, named Ⅱ-Ⅱ section. Fig. 6 depicted the strain profiles at different loading step along the width of beam top flange. It can be seen that the strain values at the beam flange welds were significantly lower than the yield strain of Q 235 steel, indicating that the RBS connection can limit strain peak value of groove welds, and thus preventing brittle fracture of the beam flange groove welds. While concentrated strains were noticed in the RBS region, leading to a plastic hinge in the RBS region.

2.2 Numerical analysis of exterior joints under beam end loading

In addition to the experimental investigation, the finite element method (FEM) was used to conduct the parametric analysis, and the ABAQUS software was selected for use in the numerical simulations of this study as it is widely used in the research center. Eight-node solid nonconforming elements C3D8I were used to reduce the number of grid units and shorten the calculation time. The plasticity model was based on the von Mises yield criteria and the associated flow rule. Mesh size varied from 2 to 10 cm in the models; a finer mesh was used in the key positions, such as the panel zone region, and the RBS regions sections to obtain the local behavior in these positions, as shown in Fig. 5(b).

2.2.1 Numerical analysis validation of exterior joint

The experimental results of specimen SJ-1 were used as a reference to validate the accuracy of FEM, and the

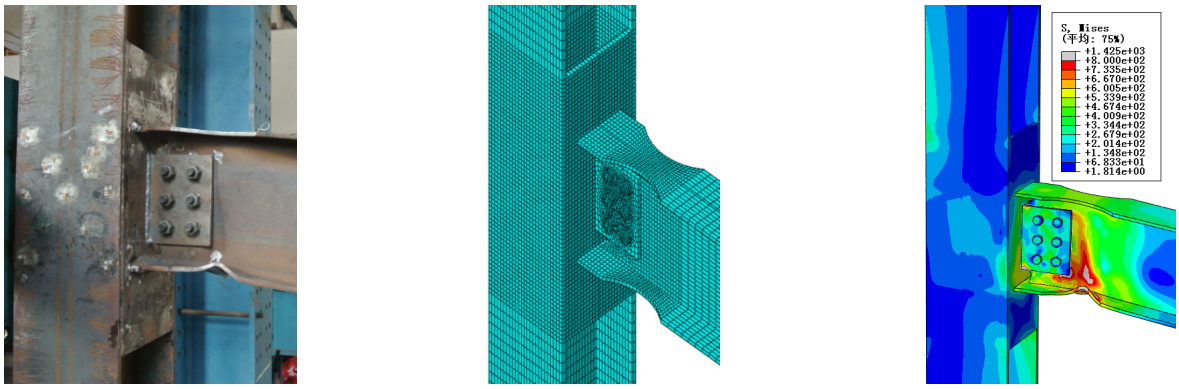

(a) Failure mode in the test (b) Meshing of the connection region (c) Failure mode in FEM

Fig. 5 Failure modes comparison of specimen SJ-1

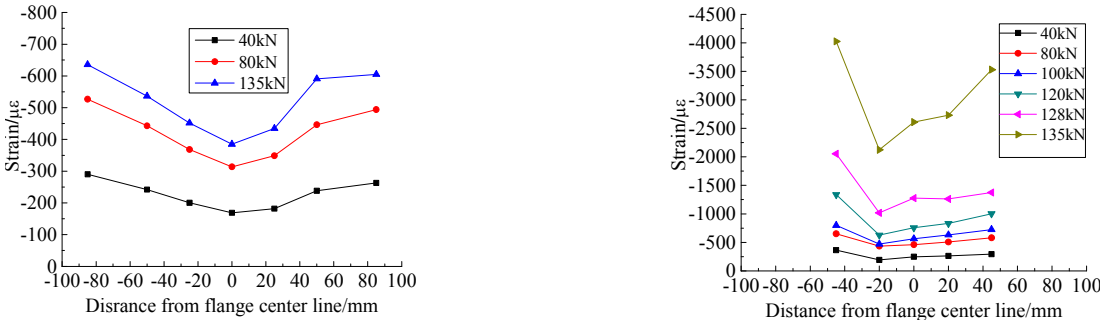

(a) I-I section (b) II-II section

Fig. 6 Strain profile along the width of beam top flange of specimen SJ-1

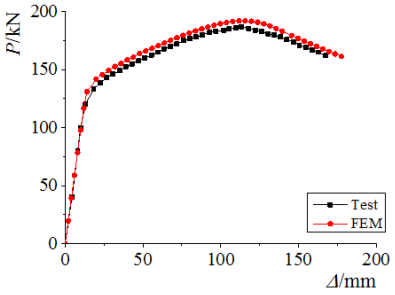

Fig. 7 *P*-Δ curves comparison of test and FEM

average material properties of steel coupons and high-strength bolt mechanical property were already presented by Lu *et al*. (2016). Failure modes comparison of test and FEM are shown in Fig. 5. It can be observed that the numerical results have good agreement with the test results in terms of failure modes.

Fig. 7 plots the load-displacement (*P*-Δ) relationships comparison of test and FEM. The initial stiffness of test and FEM matched very well and the curves showed the same trend at the plastic stage. The maximum load in FEM was slightly higher than that of the test, with an error of 2.7%, and the divergences were negligible. Overall, there was a pretty good qualitative correlation between the results of test and FEM.

2.2.2 Numerical analysis of specimen SJ-1

After validating the accuracy of the model through comparing with the full-scale test results, the specimen SJ-1 was then simulated and analyzed under beam end cyclic loading. Fig. 8 shows the failure mode, moment versus joint rotation angle (*M*-θ) relationships, and moment versus joint plastic rotation angle (*M*-θ_p) relationships of specimen SJ-1 under beam end cyclic loading. It can be seen that extensive yielding and inelastic deformation occurred in the RBS region, thus limiting the stress in the less ductile region of flange groove welds and the panel zone. The *M*-θ and *M*-θ_p hysteretic curves showed stable and reliable cyclic response, and the maximum plastic rotation angle was 0.044 rad, which satisfied the requirement of FEMA-267 (1995).

3. Experimental and numerical analysis of interior joint specimen SJ-2

3.1 Experimental analysis on interior joint under column top cyclic loading

The majority of previous tests reported were about exterior frame joints, in a practical project, however, interior frame joints are commonly used in actual engineering steel frames. In order to consider this issue, a frame interior joint specimen was constructed and loaded with the column top cyclic loading program. Fig. 9 shows the test setup of interior joint specimen SJ-2. Columns drift laterally under seismic loads in real steel frames, thus a hydraulic actuator was arranged for horizontal cyclic loading placed at the top of the column in this test program to consider the P–delta effect so as to better simulate the

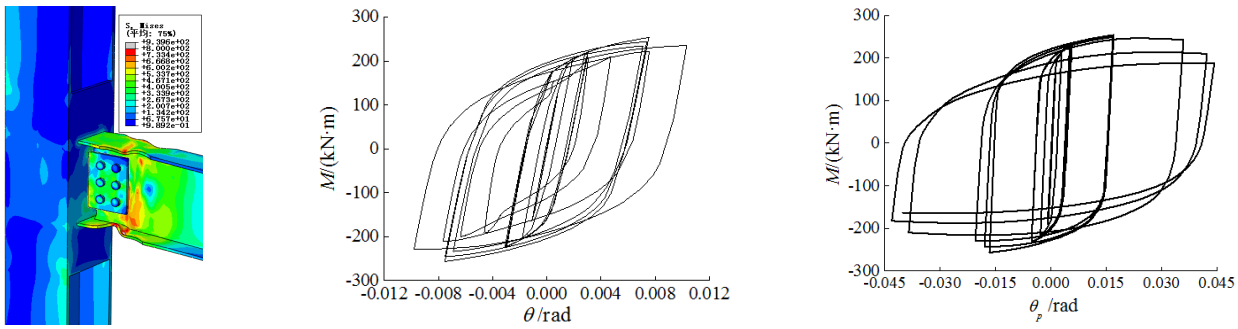

(a) Failure mode (b) *M*-θ curve (c) *M*-θ_p curve

Fig. 8 Cyclic responses of specimen SJ-1 under beam end cyclic loading

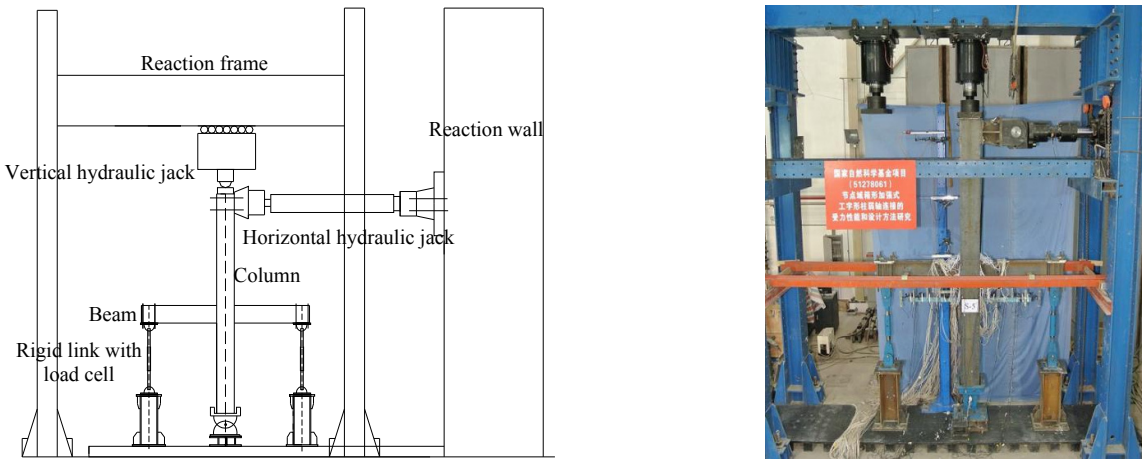

(a) Testing apparatus diagram (b) Specimen installation

Fig. 9 Test setup of specimen SJ-2

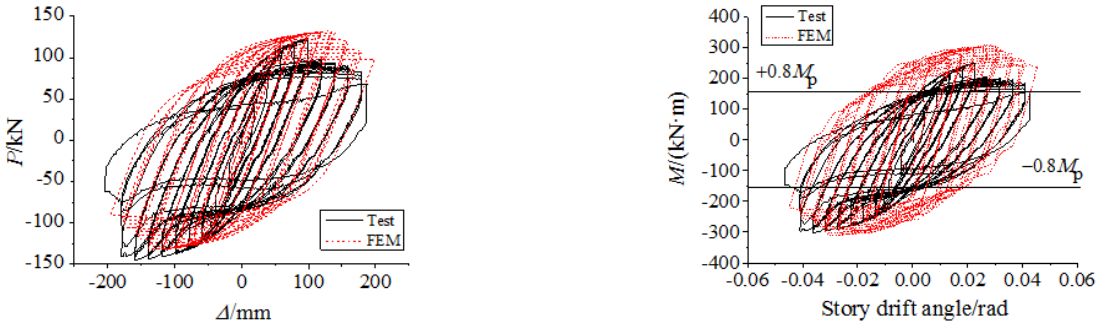

(a) Load-displacement relationships (b) Moment-story drift angle relationships

Fig. 10 Hysteretic loops of the proposed connection under cyclic loading

real situation of structural loading. Specimen SJ-2 was assembled from two 1500 mm long HN 350×175×7×11 beams and one 4030 mm height HW 350×350×12×19 column to form the cruciform arrangement, and all steel profiles were fabricated using Q235 with a nominal yield strength of 235 MPa. The beams were connected to the skin plates using the welded-flange-bolted-web connection, similar to that of the specimen SJ-1. For brevity, only the most significant results never reported are commented upon. Much additional information on the tensile test results, test phenomena, failure mode, etc., were already presented by Lu *et al*. (2017) in the companion paper.

3.1.1 Test results

The hysteretic loops of the column top load versus the controlled horizontal displacement and moment versus story drift angle are plotted in Fig. 10. It can be seen from Fig. 10(b) that the flexural resistance of specimen SJ-2 was not less than 0.80 M_p at the story drift angle of 0.04 rad, satisfying the requirements of ANSI/AISC 341-10 (2010).

The earlier web local buckling was noticed in the RBS segment during the cycles of 100 mm, followed by flange local buckling upon further loading, similar to the observation of Oh *et al*. (2015). At the first cycle of +100 mm, the positive loading achieved its peak +121.22 kN and

(a) Weld cracking between the skin plate and diaphragm (b) Weld cracking and tearing of skin plate (c) Ultimate failure mode

Fig. 11 Failure modes of specimen SJ-2

a crack appeared in the weld between the skin plate and diaphragm, as shown in Fig. 11(a), which caused a drastic drop in strength (Figs. 10(a) and (b)). In subsequent cycles, the crack developed, leading to the tearing of the skin plate ultimately (Fig. 11(b)). The ultimate failure mode was displayed in Fig. 11(c).

It can be concluded that there were much difference between column top horizontal cyclic loading and beam end monotonic or cyclic loading, the premature fracture of weld between diaphragm and skin plate caused the crack occurring early in beam flange groove weld, and prevented the development of beam plastic hinge, thus good workmanship and welding quality are first required to provide a reliable welded connection.

3.1.2 Stress profiles

3.1.2.1 Stress profile in the panel zone

Based on the measurement of strain gauge rosettes attached in the panel zone under the maximum load and the obtained steel material properties, Fig. 12(a) depicts the stress values and directions of measurement points in the panel zone. The arrow is the direction of the principal stress and the number is the stress value in MPa. It is observed from this figure that:

(1) The stress of panel zone is significantly smaller than the steel material yield strength, illustrating that only tiny elastic shear deformation occurs in the panel zone, thus it can be concluded that the proposed RBS weak-axis connection has the characteristic of strong panel zone.

(2) Relatively, larger stress appears at the two corners of one diagonal line, indicating that the larger tensile and compressive stress in the beam flange groove welds impacted the local stress distribution of panel zone.

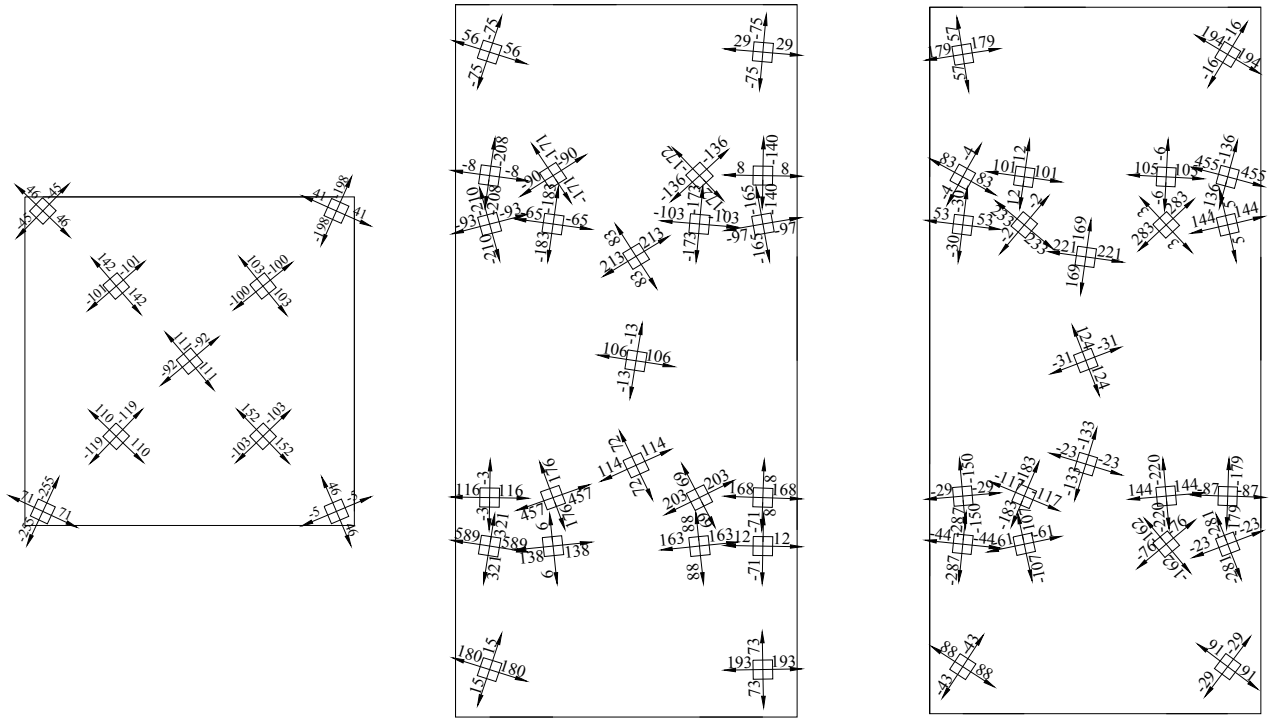

(a) Panel zone (b) Left skin plate (c) Right skin plate

Fig. 12 Stress profiles of panel zone and skin plates

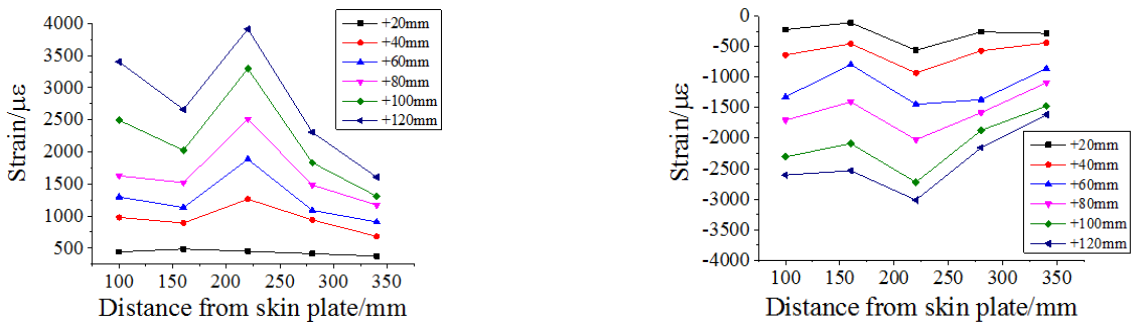

(a) The bottom flange of the left beam (b) The bottom flange of the right beam

Fig. 13 Strain profile of beam bottom flanges in specimen SJ-2

(a) Skeleton curves comparison (b) Failure mode in test (c) Failure mode in FEM

Fig. 14 Comparison of *P*-Δ skeleton curves and failure modes

3.1.2.2 Stress profile in the skin plate

The skin plate is one of the most significant elements in the proposed weak-axis connection, thus it is necessary to investigate the stress profile on the skin plates. Based on the measurement of strain gauge rosettes under the maxim load and the corresponding material properties, the stress values and directions in the skin plates for specimen SJ-2 were presented in Figs. 12(b) and (c). As can be observed from this figures that the stresses are larger where the skin plate connected to beam flanges and shear connection plate, and some values exceeded the steel material yield strength, indicating that there was still large stress concentration in the flange groove welds, leading to weld cracking and tearing of the skin plates in the test. The stresses in four corners of the skin plate, which were measured 150 mm away from the top and bottom beam flange, were relatively small and in their elastic stage, indicating that the height of skin plate, which is 200 mm away from the top and bottom beam flange, may be too large, thus the height could be reduced appropriately.

3.1.2.3 Strain profile in the steel beam flange

6 strain gauges were longitudinally located on the left and right beam bottom flanges respectively, and Fig. 13 shows strain distributions at the different loading step along the length of beam bottom flanges. It can be seen that the strain at the center of the RBS is greater than others and greater than the yield strain of Q235 steel. Therefore, it is effective to take RBS technical methods to ensure that the yielding firstly occur in the RBS region. However, there was still stress concentration in the flange groove welds. Technical methods to ensure the construction quality of the beam flange groove welds is worth considering.

3.2 Numerical analysis of interior joint under column top cyclic loading

The ABAQUS software was then used to simulate the specimen SJ-2, and the modeling methods were similar with specimen SJ-1. Fig. 10 displays the *P*-Δ and moment-story drift angle hysteretic curves comparison of test and FEM, and Fig. 14(a) shows the *P*-Δ skeleton curves comparison of test and FEM. As evidenced from Fig. 10(a) and Fig. 14, the initial stiffness, determined by the inclination of the skeleton curve in the elastic stage, of test and FEM matched well, indicating that Young's modulus and the Poisson's ratio of the material were real and effective, and the curves showed the same trend at the plastic stage. The behavior was close to that of the test in the negative direction, while the differences were more obvious in the positive direction. This was most probably due to the fact that the welds between the skin plate and diaphragm cracked, and also the flange welds, then tearing appeared in the skin plates during the test loading, leading to a large drop in resistance, which could not accurately model in FEM as the damage of steel and welds were not considered, and the material properties were simplified in the modeling, but the likelihood of fracture could be evaluated through the stress cloud in FEM. As shown in Fig. 14(c), excessive local buckling of the RBS region and concentrated stresses in the RBS region and beam flange groove welds were noticed, resulting in weld cracking and tearing of the skin plates in the experimental study. Overall, the reasonable correlation between the test and FEM was observed.

4. Parameter analysis of weak-axis RBS connections

A parametric analysis using numerical methods was conducted to determine the influence of certain parameters on the structural behavior of weak-axis RBS connections under cyclic loading. The main analyzed parameters for RBS connections are shown in Fig. 15, including the distance from skin plate to reduced beam flange zone, *a*, the length of reduced beam flange, *b*, and the depth of reduced beam flange, *c*. The modeling methods in FEM were the same as those in the reference model SJ-1 and SJ-2.

4.1 Influence of parameter a

FEMA350 (2000) recommended $a = (0.5\text{-}0.75)\ b_f$, where b_f is the beam flange width, in strong-axis RBS connections.

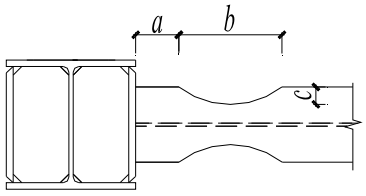

Fig. 15 Parameters in weak-axis RBS connections

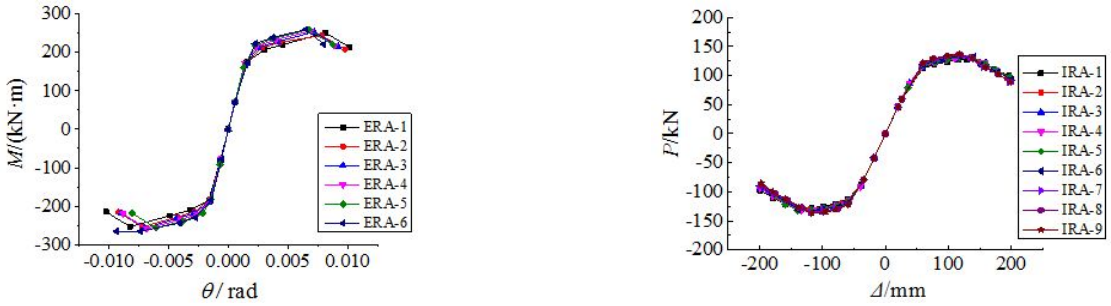

(a) *M*-*θ* skeleton curves comparison of ERA series joints (b) *P*-Δ Skeleton curves comparison of IRA series joints

Fig. 16 Skeleton curves comparison of ERA and IRA series joints

Table 1 Numerical analysis results of all series of exterior joints

	Initial rotation stiffness/(kN·m·rad^{-1})	Yield moment /(kN·m)	Yield rotation angle/rad	Ultimate moment /(kN·m)	Ultimate rotation angle/rad	Maximum plastic angle/rad	Ductility coefficient
ERA-1	120575	197.5	0.00272	213.9	0.01014	0.0391	3.73
ERA-2	123568	197.9	0.00272	214.5	0.00979	0.0449	3.60
ERA-3	125072	194.2	0.00266	215.6	0.00920	0.0443	3.46
ERA-4	126501	204.3	0.00260	218.0	0.00890	0.0428	3.42
ERA-5	129534	202.4	0.00258	220.8	0.00873	0.0424	3.38
ERA-6	131460	204.3	0.00253	220.9	0.00851	0.0386	3.36
ERB-1	122069	193.5	0.00276	213.1	0.01025	0.0388	3.71
ERB-2	124506	194.3	0.00268	215.6	0.00954	0.0438	3.56
ERB-3	125072	194.2	0.00266	215.6	0.00920	0.0443	3.46
ERB-4	132981	196.2	0.00259	214.0	0.00885	0.0428	3.42
ERB-5	134916	196.3	0.00251	213.6	0.00852	0.0412	3.39
ERB-6	139847	196.6	0.00229	213.2	0.00756	0.0376	3.30
ERC-1	139071	200.0	0.00263	228.8	0.00876	0.3650	3.33
ERC-2	129432	202.1	0.00270	224.8	0.00913	0.0396	3.38
ERC-3	125166	200.5	0.00270	219.2	0.00923	0.0432	3.42
ERC-4	125072	194.2	0.00266	215.6	0.00920	0.0443	3.46
ERC-5	120169	193.5	0.00260	211.6	0.00915	0.0417	3.52
ERC-6	116222	190.3	0.00252	198.1	0.00910	0.0371	3.61
EST-1	125072	194.2	0.00266	215.6	0.00920	0.0443	3.46
EST-2	120643	193.0	0.00275	214.0	0.00901	0.0401	3.28
EST-3	115978	190.9	0.00278	212.3	0.00871	0.0346	3.13
EST-4	111110	187.1	0.00293	210.5	0.00865	0.0296	2.95
ESM-1	126807	311.8	0.00262	354.7	0.00910	0.0429	3.47
ESM-2	122888	301.4	0.00271	332.9	0.00931	0.0396	3.43

In order to investigate the influences of the parameter *a* on the mechanical behavior of weak-axis RBS connection, six exterior joint models (ERA series) and nine interior joint models (IRA series) will be compared and analyzed, and all the other conditions are kept the same as the reference model. Attached List shows the details of those frame joints.

4.1.1 Influences on exterior joints

ERA series exterior joints were investigated under beam end cyclic loading, and their *M*-*θ* skeleton curves comparison are shown in Fig. 16(a), and the mechanical properties are summarized in Table 1. It can be obtained that increasing the parameter *a* could result in slightly larger initial rotation stiffness and bearing capacity, and obvious smaller ductility. Moreover, for the maximum plastic rotation angle, there is a trend of early rising and later falling. Although the maximum plastic rotation angle of all the specimens was greater than 0.03 rad, the limit value of FEMA267 (1995), the exterior joints showed better mechanical performance when the parameter *a* satisfied the requirement of FEMA350 (2000).

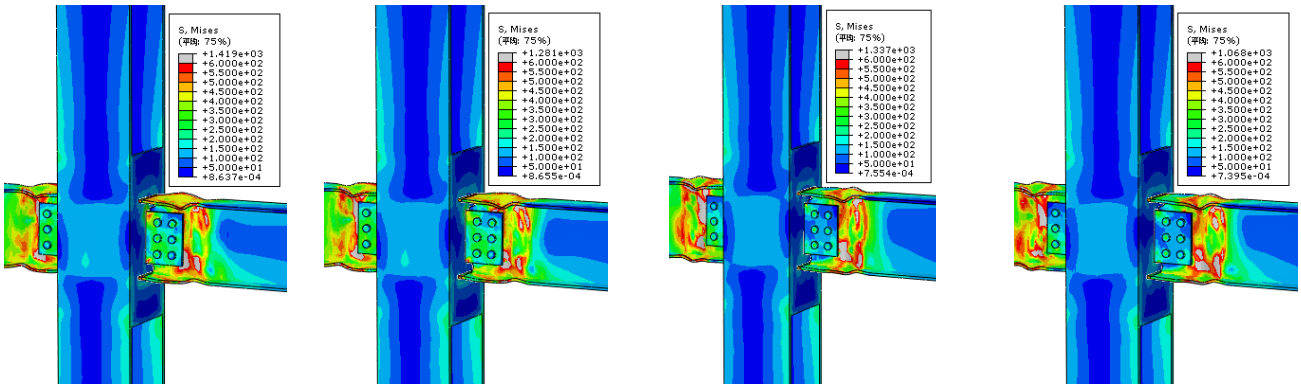

(a) IRA-3 (b) IRA-4 (c) IRA-7 (d) IRA-8

Fig. 17 Stress profile of parts of IRA series specimen

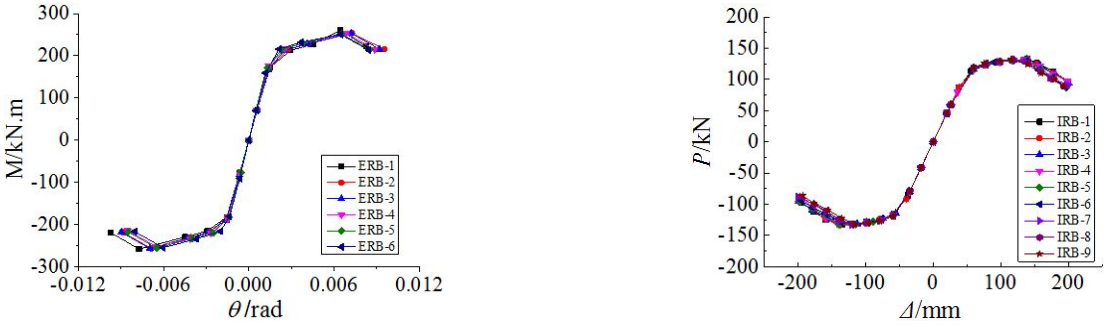

(a) Skeleton curves of ERB series joints (b) Skeleton curves of IRB series joints

Fig. 18 Skeleton curves of ERB and IRB series joints

4.1.2 Influence on interior joints

IRA series interior joints were analyzed under column top cyclic loading, and their *P*-Δ Skeleton curves comparison is shown in Fig. 16(b). Failure modes comparison is shown in Fig. 17. Furthermore, Table 2 summarizes their numerical analysis results. It can be seen that the influences of the parameter *a* on the stiffness, bearing capacity and ductility are the same as exterior joints. The failure modes illustrated that the beam plastic hinge was more closely to the panel zone and the stress of the beam groove weld was higher when the value of the parameter *a* was less than the limit value of FEMA350 (2000).

In summary, the stiffness and bearing capacity of frame joints were not very sensitive to the variation of parameter *a*. While on one hand, the larger the parameter *a*, the smaller the ductility of frame joints, and on the other hand, too small value of parameter *a* would increase the risk of flange welds fracture. Therefore, it is reasonable to use a = (0.55~0.75) b_f for design purposes of weak-axis RBS connections.

4.2 Influence of parameter b

FEMA350 (2000) recommended b = (0.65-0.85) h_b, where h_b is the beam depth, in strong-axis RBS connections. Based on the recommendations, fifteen models were designed to discuss the effect of parameter *b* on the mechanical behavior of weak-axis RBS connection, including six exterior joint models (ERB series) and nine interior joint models (IRB series). Attached List shows the details of these fifteen joints.

4.2.1 Influence on exterior joints

ERB series exterior joints were investigated under beam end cyclic loading, and their *M*-*θ* skeleton curves comparison is shown in Fig. 18(a), and the mechanical properties are summarized in Table 1. It can be obtained that increasing the parameter *b* could result in slightly larger initial rotation stiffness and obvious smaller ductility, and the bearing capacity was insensitive to the variation of the parameter *b*. Similar to the influence of parameter *a*, there is a trend of early rising and later falling for the maximum plastic rotation angle. Although the maximum plastic rotation angle of all the specimens was greater than 0.03 rad, the limit value of FEMA267 (1995), the exterior joints showed better mechanical performance when the parameter *b* satisfied the requirement of FEMA350 (2000).

4.2.2 Influence on interior joints

IRB series frame joints were analyzed under column top cyclic loading and their *P*-Δ Skeleton curves comparison is shown in Fig. 18(b). Failure modes comparison is shown in Fig. 19. Furthermore, Table 2 gives the numerical analysis results of these joints. It can be seen that little deviation was observed in the stiffness and the bearing capacity. While as the parameter *b* increased the ductility decreased. The failure modes illustrated that the stress of the beam groove

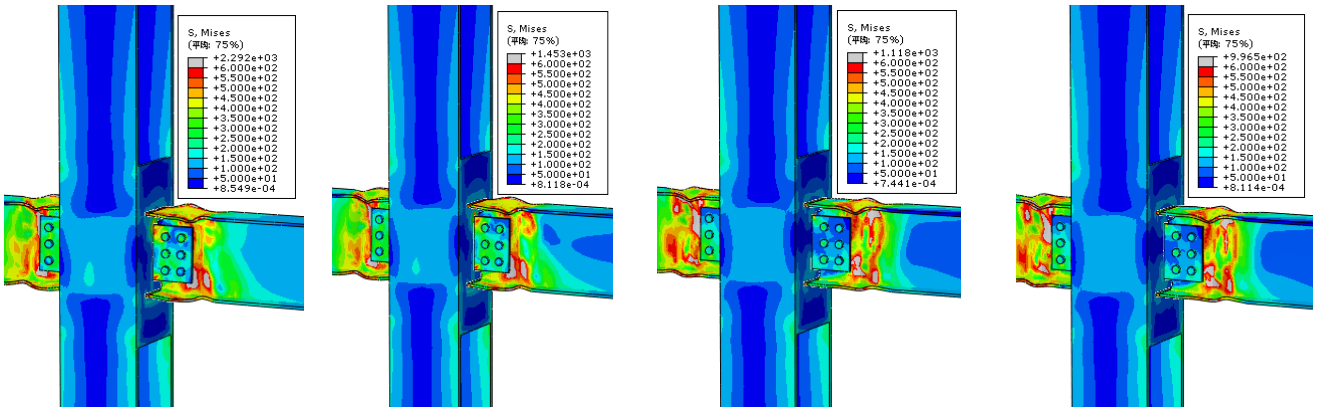

(a) IRB-2 (b) IRB-3 (c) IRB-7 (d) IRB-8

Fig. 19 Stress profile of parts of IRB series specimen

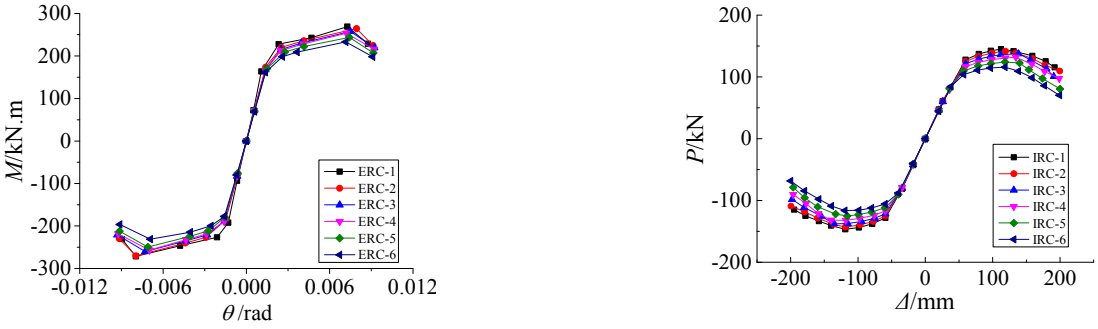

(a) Skeleton curves of ERC series joints (b) Skeleton curves of IRC series joints

Fig. 20 Skeleton curves of ERC and IRC series joints

welds was higher when the value of the parameter b was less than the limit value of FEMA350 (2000).

In summary, the stiffness and bearing capacity of frame joints were not very sensitive to the variation of parameter b. While on one hand, the larger the parameter b, the smaller the ductility of frame joints, and on the other hand, too small value of parameter b would increase the risk of flange welds fracture. Therefore, it is reasonable to use b = (0.65-0.85) h_b for design purposes of weak-axis RBS connections.

4.3 Influence of parameter c

The parameter c reflects the depth of reduced beam flange. Obviously, larger parameter c will help the formation of plastic hinges, meanwhile, decrease the bearing capacity. FEMA350 (2000) recommended c = (0.2-0.25) b_f, where b_f is the beam flange width, in strong-axis RBS connections. Based on the recommendations, twelve models were designed to discuss the effect of parameter c on the mechanical behavior of weak-axis RBS connection,

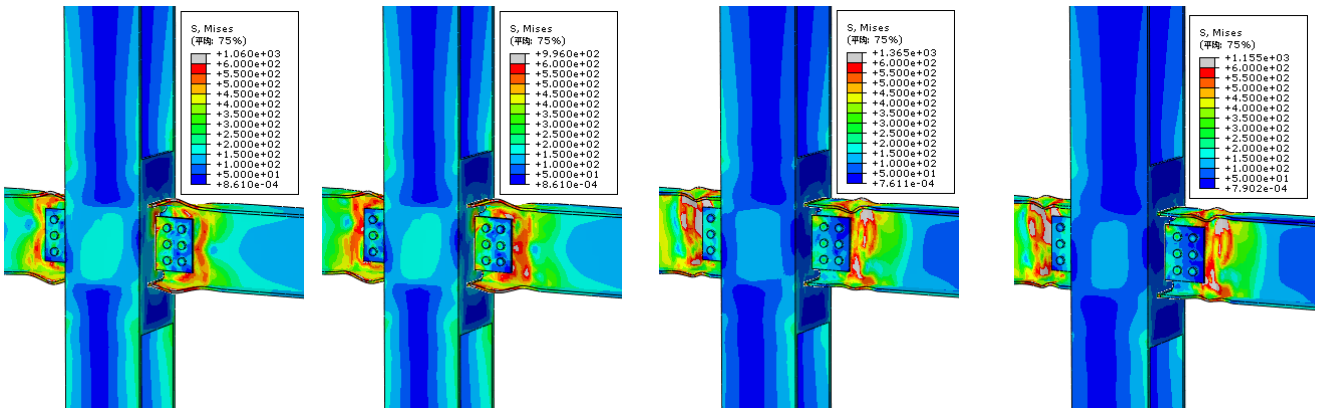

(a) IRC-1 (b) IRC-2 (c) IRC-5 (d) IRC-6

Fig. 21 Stress profile of parts of IRC series specimen

Table 2 Numerical analysis results of all series of interior joints

	Yield load /kN	Yield displacement /mm	Peak load /kN	Peak displacement /mm	Ultimate load /kN	Ultimate displacement /mm	Ductility coefficient
IRA-1	100.25	55.90	127.91	138.75	108.72	176.64	3.16
IRA-2	102.58	56.99	130.64	137.52	111.04	176.67	3.10
IRA-3	103.17	57.01	130.78	136.46	111.16	174.45	3.06
IRA-4	104.91	57.36	131.63	135.39	111.89	172.65	3.01
IRA-5	105.37	57.50	132.03	136.33	112.23	171.25	2.98
IRA-6	107.16	57.67	132.65	119.83	112.76	160.53	2.78
IRA-7	109.25	58.40	134.59	118.32	114.40	155.38	2.66
IRA-8	110.19	59.06	136.21	117.82	115.78	152.07	2.57
IRA-9	112.21	59.27	136.75	117.31	116.23	150.25	2.54
IRB-1	104.75	57.62	132.80	139.54	112.88	177.79	3.09
IRB-2	105.29	57.58	132.46	138.91	112.69	175.38	3.05
IRB-3	105.82	57.55	132.39	138.26	112.53	173.51	3.02
IRB-4	105.37	57.50	132.03	136.33	112.23	171.25	2.98
IRB-5	105.04	56.95	130.55	136.09	110.97	165.44	2.91
IRB-6	106.38	57.26	131.04	119.60	111.38	161.23	2.82
IRB-7	105.13	57.50	131.36	118.91	111.65	158.97	2.76
IRB-8	105.75	57.66	131.57	117.70	111.83	156.81	2.72
IRB-9	105.36	57.70	131.50	115.19	111.78	153.28	2.66
IRC-1	123.75	61.50	146.11	139.02	124.19	178.38	2.90
IRC-2	121.00	60.43	141.63	137.17	120.39	175.18	2.90
IRC-3	116.25	59.25	137.48	135.63	116.86	172.50	2.91
IRC-4	105.37	57.50	132.03	136.33	112.23	171.25	2.98
IRC-5	101.15	54.66	124.02	118.79	105.42	162.40	2.97
IRC-6	97.40	51.72	115.75	118.34	98.39	158.57	3.07
IST-1	104.82	60.20	129.45	137.21	110.03	172.56	2.87
IST-2	105.37	57.50	132.03	136.33	112.23	171.25	2.98
IST-3	106.63	55.32	132.29	133.53	112.45	168.75	3.05

including six exterior joint models (ERC series) and six interior joint models (IRC series). Attached List shows the details of these twelve joints.

4.3.1 Influences on exterior joints

ERC series exterior joints were investigated under beam end cyclic loading, and their M-θ skeleton curves comparison is shown in Fig. 20(a), and the mechanical properties are summarized in Table 1. It can be obtained that increasing the parameter c could result in smaller initial rotation stiffness and bearing capacity, and larger ductility. Similar to the influence of parameters a and b, there is a trend of early rising and later falling for the maximum plastic rotation angle. Although the maximum plastic rotation angle of all the specimens was greater than 0.03 rad, the limit value of FEMA267 (1995), the exterior joints showed better mechanical performance when the parameter c satisfied the requirement of FEMA350 (2000).

4.3.2 Influence on interior joints

IRC series frame joints were analyzed under column top cyclic loading and their P-Δ Skeleton curves comparison is shown in Fig. 20(b). Failure modes comparison is shown in Fig. 21. Furthermore, Table 2 gives the numerical analysis results of these joints. It can be seen that the influences of the parameter c on the stiffness, bearing capacity and ductility were the same as exterior frame joints. The failure modes illustrated that the stress of the beam groove welds was higher when the value of the parameter c was less than the limit value of FEMA350 (2000).

In summary, the increasing of the parameter c can obviously decrease the initial rotation stiffness and bearing capacity but increase the ductility. When the parameter c coincides the suggestions of FEMA350 (2000), the weak-axis RBS connections showed satisfactory hysteretic performance.

5. Calculation formula of skin plate thickness

The out-of-plane stiffness of skin plate, decided mainly by the thickness of skin plate, is very small compared to the plane stiffness, but it has great influence on the joint rotation stiffness and the formation of plastic hinges.

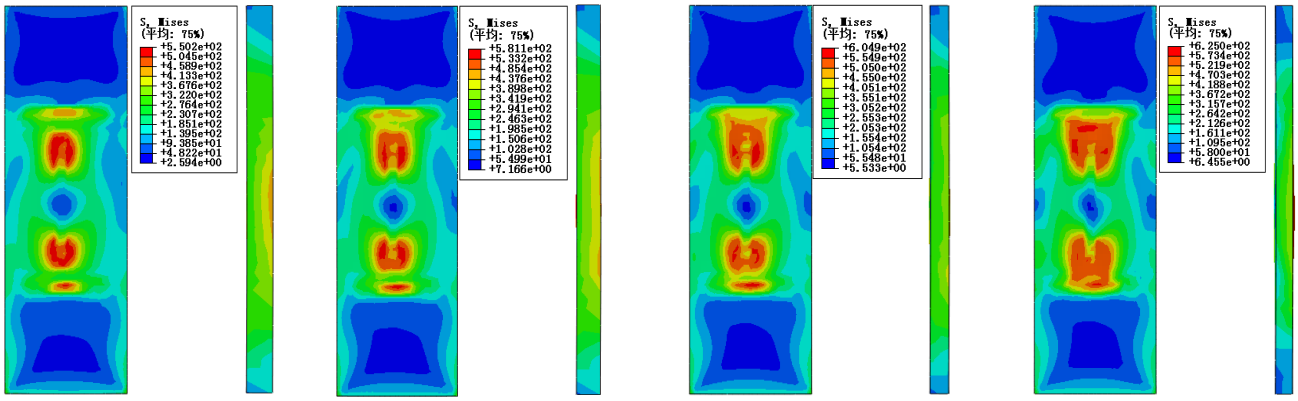

(a) EST-1 (b) EST-2 (c) EST-3 (d) EST-4

Fig. 22 Stress profiles of skin plates of EST series joints

Generally, the beam-column connection with thicker skin plate has the higher bearing capacity, while thinner steel plate has better metal quality. In order to seek for the most suitable thickness of skin plate, according to the experimental models and referring the formula of thethickness of panel zone which is written in the Section 8.2.5 of the Code GB 50011-2010 (2010), a calculation formula of skin plate thickness t_s in a weak-axis RBS connection is given as follow.

$$t_s \geq \frac{h_c + h_b}{60}\sqrt{\frac{235}{f_y}} \quad (1)$$

Where h_b is the beam depth; h_c is the column depth; f_y is the normal yield strength of steel material used in the connection.

5.1 Formula validation for exterior joints

EST series models were exterior joint models with the thickness of skin plate changing, and all the other conditions were kept the same as specimen SJ-1. According to Eq. (1), the minimum thickness of specimen SJ-1 is 11 mm, four exterior joint models were created, and their details are shown in Attached List. The failure modes were similar to specimen SJ-1, and stress clouds of skin plates of EST series joints are displayed in Fig. 22, and Table 1 lists the numerical analysis results. It can be observed from those figures and data that:

(1) The thicker the skin plate, the larger stress profiles in the skin plate.
(2) Increasing the thickness of skin plate thickness from 10 mm to 16 mm slightly affected the bearing capacity, but strongly affected the stiffness, ductility, and maximum plastic rotation angle. The initial rotation stiffness of EST-1 is 12.6% greater than EST-4, the ductility coefficient of EST-4 is 26.8% higher than EST-1, and the maximum plastic rotation angle of EST-1 is 12.2% greater than EST-4.
(3) The maximum plastic rotation of EST-4, with 10 mm thickness skin plate, did not satisfy the requirement of FEMA267 (1995), while other models with the thickness of skin plate larger than 11 mm, calculated by Eq. (1), could reach 0.03 rad plastic rotation. Thus, the Eq. (1) is suitable to calculate skin plate thickness for weak-axis RBS exterior joints.

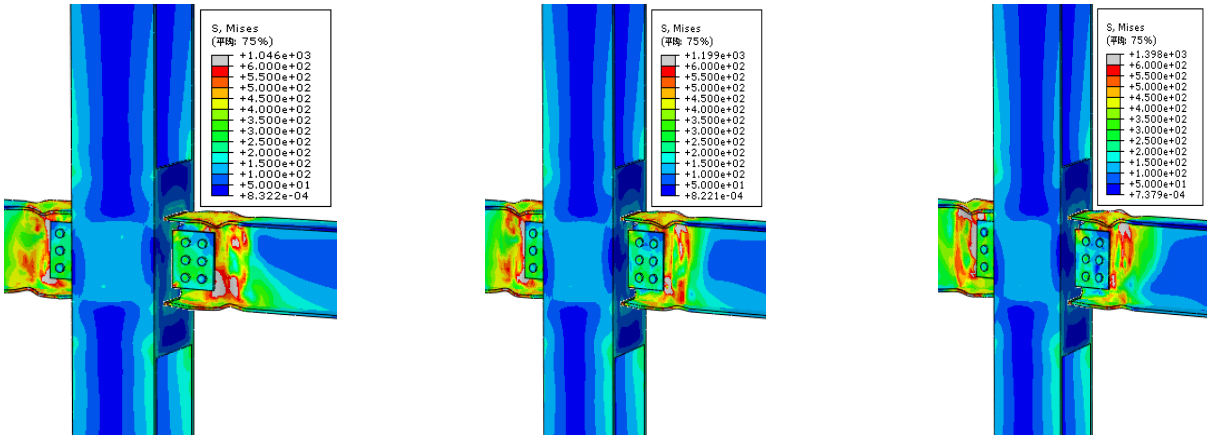

(a) IST-1 (b) IST-2 (c) IST-3

Fig. 23 Failure modes of IST series joints

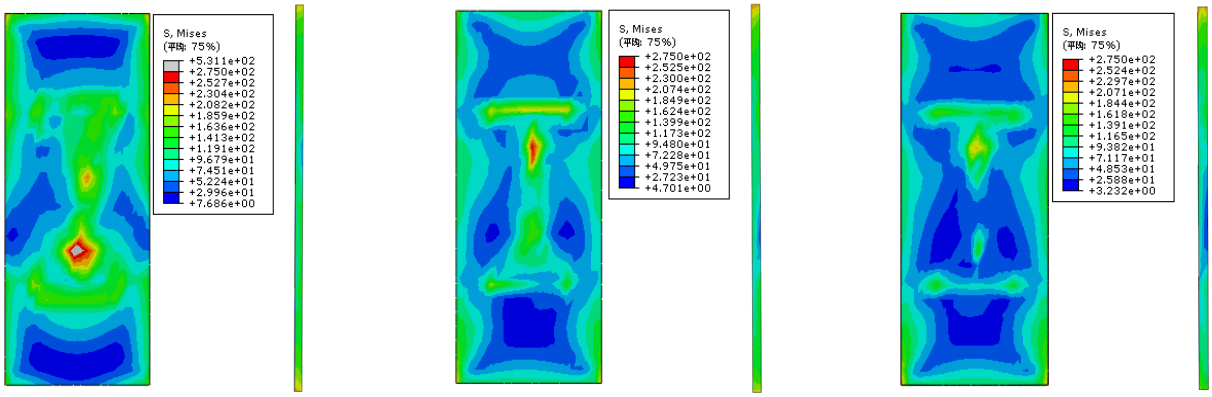

(a) IST-1 (b) IST-2 (c) IST-3

Fig. 24 Stress profiles of skin plates of IST series joints

5.2 Formula validation for interior joints

IST series models were interior joint models with the thickness of skin plate changing, and all the other conditions were kept the same as specimen SJ-2. Details are displayed in Attached List. According to Eq. (1), the minimum thickness of IST series joints is 12 mm, and all IST series models satisfied Eq. (1). The failure modes and stress clouds of skin plates are displayed in Figs. 23 and 24 respectively, and the numerical analysis results are listed in Table 2. It can be obtained from those figures and data that:

(1) IST series models can provide enough stiffness to compel beam to form a plastic hinge, the plastic hinge occurred at RBS region and a low-stress zone existed in the beam flange groove weld. Similar to EST series joints, the peak Mises stress of IST-1 is 1.9-times of IST-3.
(2) The thickness change of skin plate gently influences the stiffness, bearing capacity and joint ductility when the minimum thickness of skin plate satisfies Eq. (1).
(3) Eq. (1) is suitable to calculate the minimum skin plate thickness for weak-axis RBS interior joints.

5.3 Formula validation in different steel grade

Using the true coupon test material properties, grade Q345 whose yield strength is 333.33 MPa, and tensile strength is 458.33 MPa, and Elastic modulus is 2.06×10^5 MPa, and Elongation is 21.9%. ESM series joints, total two exterior frame joints were analyzed under beam end cyclic loading in order to investigate the applicability of Eq. (1) for different steel grade except for grade 235. Details are displayed in Attached List. According to Eq. (1), the minimum thickness of ESM series joints is almost 14 mm. The failure modes of these joints are displayed in Fig. 25 and the numerical analysis results are listed in Table 1. It can be obtained from those figures and data that:

(1) The overall failure modes of the ESM series joints nearly resemble, and the plastic hinges formed at the RBS regions. The stress values in skin plates increased with the decrease of the skin plate thickness.
(2) Changing the thickness of skin plate slightly affected the bearing capacity, stiffness, ductility coefficient and maximum plastic rotation angle when the minimum thickness of skin plate satisfies Eq. (1). Therefore, Eq. (1) is suitable to calculate skin plate thickness for different grade steel whose normal yield strength between 235 MPa and 345 MPa.

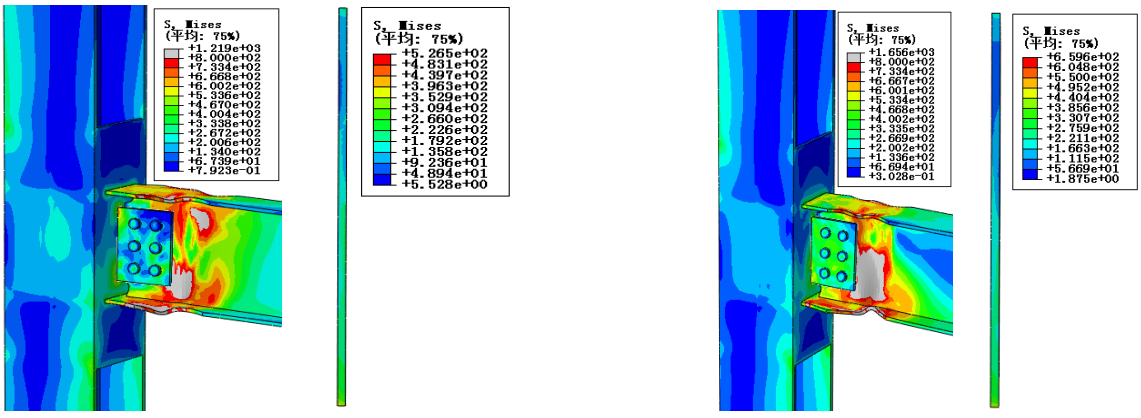

(a) ESM-1 (b) ESM-2

Fig. 25 Failure modes of ESM series joints

6. Recommended design procedure

Based on test design of the past, as well as the analytical parametric studies conducted, the following design procedure was developed for weak-axis RBS moment connections, when column and beam sections had been determined. Part of the design steps derives from FEMA350 (2000).

Step 1: Design of skin plate

The geometrical size of skin plate is determined by column section and beam section. Skin plate width equals to the column section height minus the sum of the two column flange thickness, and skin plate minimum height equals to the beam section height plus 300 mm, and skin plate thickness is calculated by Eq. (1).

Step 2: Design of reduced parameter

For the three parameters shown in Fig. 15, according to the experimental tests and numerical analysis, a = (0.55-0.75) b_f and b = (0.65-0.85) h_b and c = (0.2-0.25) b_f. Where b_f is the width of beam flange and h_b is the beam depth.

Step 3: Determine probable plastic moment at hinges

For fully restrained connections designed to develop plastic hinging in the beam or girder, the probable plastic moment at the location of the plastic hinge should be determined as

$$M_{pr} = C_{pr} R_y W_{pe} F_y \tag{2}$$

Where, M_{pr} is probable peak plastic hinge moment; C_{pr} = a factor to account for the peak connection strength, including strain hardening, local restraint, additional reinforcement, and other connection conditions. For most connection types, C_{pr} is given by the formula (3); R_y = a coefficient, applicable to the beam or girder material, a value of 1.1 may be used for all cases; W_{pe} = the effective plastic modulus of the reduced section of the beam; F_{yb} = the specified minimum yield stress of the material of the beam; F_{ub} = the specified minimum tensile stress of the material of the beam.

$$C_{pr} = \frac{F_{yb} + F_{ub}}{2F_{yb}} \tag{3}$$

Step 4: Determine shear at the plastic hinge

The shear V_P at the plastic hinge should be determined by methods of statics, considering gravity loads acting on the beam. A free body diagram of that portion of the beam between plastic hinges is a useful tool for obtaining the shear at each plastic hinge. Fig. 26 provides an example of such a calculation. For the purposes of such calculations, gravity load should be based on the load combinations indicated in Section 3.4.1 (FEMA350, 2000).

Step 5: Determine strength demands at each critical section

In order to complete the design of the connection, including, for example, sizing the shear connection plates, bolts, and joining welds which make up the connection, it is necessary to determine the shear and flexural strength demands at the critical section that is at the skin plate face.

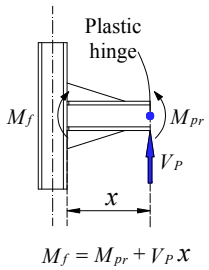

Fig.26 Calculation of demands at critical sections

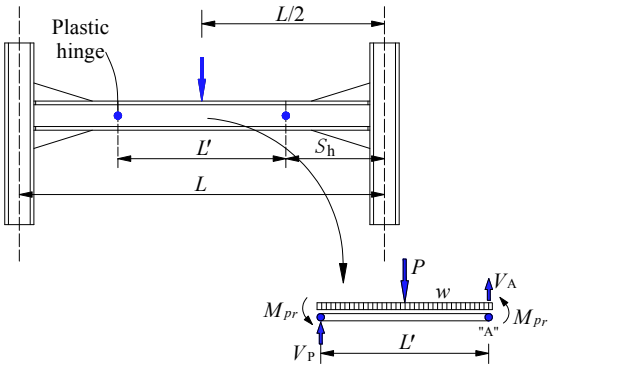

Fig.27 Sample calculation of shear at plastic hinge

These demands may be calculated by taking a free body of that portion of the connection assembly located between the critical section and the plastic hinge. Fig. 26 demonstrates this procedure for the critical sections, for the beam shown in Fig. 27.

Step 6: Check parameter c

Calculate M_f according to the method of Step 5 and Fig. 27 using C_{pr} = 1.15. If $M_f < C_{pr} R_y W_{pb} F_{yb}$ the design is acceptable and turn to Step 7. If M_f is greater than the limit c should be increased to satisfy $M_f < C_{pr} R_y Z_b F_y$. The value of c should not exceed 0.25 b_f. Where, R_y = a coefficient, applicable to the beam or girder material, a value of 1.1 may be used for all cases; W_{pb} = the plastic modulus of the beam section; F_{yb} = the specified minimum yield stress of the material of the beam.

Step 7: Calculate the shear at the skin plate face

The shear is calculated according to the equation

$$V_f = 2\frac{M_f}{L - h_c} + V_g \tag{4}$$

Where, V_g = shear due to factored gravity load, and it is calculated according to Fig. 26; L = the span of the beam and is shown in the Fig.26; h_c = the column depth.

Step 8: Design the shear connection of the beam to the column

If a CJP welded web is used, no further calculations are required. If a bolted shear tab is to be used, the tab and bolts should be designed and the shear force is calculated in Step 7.

Step 9: Design groove weld

In China, the "V" groove weld of beam flange does not require calculation, when the quality grade is one or two. But it is necessary to take some technical methods to ensure the construction quality of the beam flange groove weld. Use a backing plate and remove it after groove weld is in place and weld metal deposition become cool, and then the edges of the groove weld should be ground smooth to avoid notches.

Step 10: Strong column-weak beam criterion

According to GB50011-2010 (2010), strong column-weak beam criterion is displayed by Eq. (5) shown as follow.

$$\sum W_{pc}\left(f_{yc}-N/A_c\right)\geq \eta\sum W_{pb}f_{yb} \tag{5}$$

Where, W_{pc} = plastic section modulus of the column section; W_{pb} = plastic section modulus of the beam section; f_{yc} = the yield stress of column; f_{yb} = the yield the material of the beam; N = the axial force on column in compression considering earthquake action; A_c = the gross area of column; η = a coefficient given in GB50011-2010 (2010).

Step 11: Panel zone check

According to GB50011-2010 (2010), make sure that the yield bearing capacity and design bearing capacity of panel zone satisfy Eqs. (6) and (7). Since the panel zone is composed of two flanges, the panel zone strength requirement is usually easily satisfied.

$$\psi\left(M_{\mathrm{pb1}}+M_{\mathrm{pb2}}\right)/(1.8h_{b1}h_{c1}t_w)\leq(4/3)f_{\mathrm{yv}} \tag{6}$$

$$\left(M_{\mathrm{b1}}+M_{\mathrm{b2}}\right)/(1.8h_{b1}h_{c1}t_w)\leq(4/3)f_{\mathrm{v}}/\gamma_{\mathrm{RE}} \tag{7}$$

Where, h_{b1} = the distance between the center of top and bottom beam flange; h_{c1} = the distance between the centers of column flange; t_{w} = thickness of column flange; M_{pb1} and M_{pb2} = the full plastic bending bearing capacity of both sides beam respectively; Ψ = a factor given in GB50011-2010 (2010); f_{yv} = the yield shear strength of steel; M_{b1} and M_{b2} = the design moment of both sides beam respectively; f_{yv} = the design shear strength of steel; γ_{RE} = a coefficient considers earthquake action and equals to 0.75.

7. Conclusions

This paper systematically investigated the hysteretic performance of the weak-axis RBS connections using the test and FEM methods. Based on the experimental and numerical analysis results, the following conclusions can be made about the novel weak-axis RBS moment connections.

- The RBS could reduce the peak stress of groove welds efficiently and thus prevent brittle weld fracture in both weak-axis RBS connection specimens tested, even though the construction quality of weld between the diaphragm and skin plate was poor. But good workmanship and welding quality are still firstly required to provide a reliable welded connection.
- The proposed weak-axis RBS connection has a strong panel zone. The tested specimens could meet the requirements of FEMA-267 (1995) and ANSI/AISC 341-10 (2010) for special moment frame connections, indicating the proposed weak-axis RBS connections has a lot of potential for using in the engineering projects.
- The rules recommended by FEMA350 (2000) for RBS parameters are also suitable for the proposed weak-axis RBS moment connection.
- Eq. (1) is suitable to calculate the minimum skin plate thickness for the proposed weak-axis RBS connections for different grade steel with normal yield strength between 235 and 345 MPa.
- A design procedure is recommended for the weak-axis RBS moment connections.

Acknowledgments

The authors would like to thank the Nature Science Foundation of China (NSFC) (51278061) and the Fundamental Research Funds for the Central Universities-Cultivation of Chang'an University (300102288201) for the financial support. And opinions, findings, conclusions and recommendations expressed in this paper are those of the writers and do not necessarily reflect the views of the sponsors.

References

ANSI/AISC 341-10 (2010), Seismic Provisions for structural steel buildings. AISC; Chicago, IL, USA.

Chen, S.J., Yeh, C.H. and Chu, J.M. (1996), "Ductile steel beam-to-column connections for seismic resistance", *J. Struct. Eng.*, **122**(11), 1292-1299.

Crisan, A. and Dubina, D. (2016), "Bending–shear interaction in short coupling steel beams with reduced beam section", *J. Constr. Steel Res.*, **122**, 190-197.

Driscoll, G.C. and Beddle, L.S. (1982), "Suggestions for avoiding beam-to-column web connection failure", *Eng. J.*, **19**, 16-19.

FEMA-267 (1995), Interim Guidelines: Evaluation, Repair, Modification and Design of Steel Moment Frames, Report No. SAC-95-02; Washington, D.C., USA.

FEMA-350 (2000), Recommended Seismic Design Criteria for New Steel Moment-Frame Buildings, Prepared for SAC Joint Venture Partnership by Guidelines Development Committee, Washington, D.C., USA

FEMA-355D (2000), State of the Art Report on Connection Performance, prepared by the SAC Joint Venture for the Federal Emergency Management Agency, Washington, WA, USA.

GB 50011-2010(2010), Code for Seismic Design of Buildings, China Architecture & Building Press; Beijing, P.R. China.

Gilton, C.S. and Uang, C.M. (2002), "Cyclic Response and Design

Recommendations of Weak-Axis Reduced Beam Section Moment Connections", *J. Struct. Eng.*, **128**(4), 452-463.
Lee, C.H., Jung, J.H. and Kim, S.Y. (2015), "Cyclic Seismic Performance of RBS Weak-Axis Welded Moment Connections", *J. Korean Soc. Steel Constr.*, **27**(6), 513-523.
Lignos, D., Kolios, D. and Miranda, E. (2010), "Fragility Assessment of Reduced Beam Section Moment Connections", *J. Struct. Eng.*, **136**(9), 1140-1150.
Lu, L.F., Xu, Y.L., Zhou, T.H. and Zheng H. (2016), "Experimental research on box strengthened joint connection for weak-axis of I-section column H-shaped beam under monotonic loading", *J. Build. Struct.*, **37**(2), 73-80.
Lu, L.F., Xu, Y.L. and Zheng, H. (2017), "Investigation of composite action on seismic performance of weak-axis column bending connections", *J. Constr. Steel Res.*, **129**, 286-300.
Lu, L.F., Xu, Y.L. and Lim, J.B.P. (2018), "Mechanical performance of a new I-section weak-axis column bending connection", *Steel Compos. Struct., Int. J.*, **26**(1), 31-44.
Oh, K., Lee, K., Chen, L., Hong, S.B. and Yang, Y. (2015), "Seismic performance evaluation of weak axis column-tree moment connections with reduced beam section", *J. Constr. Steel Res.*, **105**, 28-38.
Rezaifar, O. and Younesi, A. (2016), "Finite element study the seismic behavior of connection to replace the continuity plates in (NFT/CFT) steel columns", *Steel Compos. Struct., Int. J.*, **21**(1), 73-91.
Uniform Building Code (1994), International Conference of Building Officials, Whittier, CA, USA
Xu, Y.L., Lu, L.F. and Ma, P.B. (2016), "Finite element analysis on the hysteretic behavior of box strengthen-joint region connection between minor-axis I-shaped column and strengthen-weaken beam", *Progress in Steel Building Structures*, **18**(2), 17-25.
Zahrai, S.M., Mirghaderi, S.R. and Saleh, A. (2017a), "Increasing plastic hinge length using two pipes in a proposed web reduced beam section, an experimental and numerical study", *Steel Compos. Struct., Int. J.*, **23**(4), 421-433.
Zahrai, S.M., Mirghaderi, S.R. and Saleh, A. (2017b), "Tubular Web Reduced Beam Section (TW-RBS) connection, a numerical and experimental study and result comparison", *Steel Compos. Struct., Int. J.*, **23**(5), 571-583.
Zhou, T.H. and Zheng, H. (2016), "Experimental research on box strengthened joint connection for weak axis of I-section column-H-shaped beam under monotonic loading", *J. Build. Struct.*, **37**(2), 73-80.

CC

Attached List

Member	Section of column	Section of beam	Skin plate	Diaphragm	*a*/mm	*b*/mm	*c*/mm
ERA-1	HW300×300×10×15	HN350×175×7×11	-270×750×16	-129×270×12	**0.40b_f=70**	0.69h_b=240	0.23b_f=40
ERA-2	HW300×300×10×15	HN350×175×7×11	-270×750×16	-129×270×12	**0.51b_f=90**	0.69h_b=240	0.23b_f=40
ERA-3	HW300×300×10×15	HN350×175×7×11	-270×750×16	-129×270×12	**0.57b_f=100**	0.69h_b=240	0.23b_f=40
ERA-4	HW300×300×10×15	HN350×175×7×11	-270×750×16	-129×270×12	**0.66b_f=115**	0.69h_b=240	0.23b_f=40
ERA-5	HW300×300×10×15	HN350×175×7×11	-270×750×16	-129×270×12	**0.74b_f=130**	0.69h_b=240	0.23b_f=40
ERA-6	HW300×300×10×15	HN350×175×7×11	-270×750×16	-129×270×12	**0.86b_f=150**	0.69h_b=240	0.23b_f=40
ERB-1	HW300×300×10×15	HN350×175×7×11	-270×750×16	-129×270×12	0.57b_f=100	**0.57h_b=200**	0.23b_f=40
ERB-2	HW300×300×10×15	HN350×175×7×11	-270×750×16	-129×270×12	0.57b_f=100	**0.66h_b=230**	0.23b_f=40
ERB-3	HW300×300×10×15	HN350×175×7×11	-270×750×16	-129×270×12	0.57b_f=100	**0.69h_b=240**	0.23b_f=40
ERB-4	HW300×300×10×15	HN350×175×7×11	-270×750×16	-129×270×12	0.57b_f=100	**0.77h_b=270**	0.23b_f=40
ERB-5	HW300×300×10×15	HN350×175×7×11	-270×750×10	-129×270×12	0.57b_f=100	**0.83h_b=290**	0.23b_f=40
ERB-6	HW300×300×10×15	HN350×175×7×11	-270×750×12	-129×270×12	0.57b_f=100	**0.91h_b=320**	0.23b_f=40
ERC-1	HW300×300×10×15	HN350×175×7×11	-270×750×14	-129×270×12	0.57b_f=100	0.69h_b=240	**0.18b_f=32**
ERC-2	HW300×300×10×15	HN350×175×7×11	-270×750×16	-129×270×12	0.57b_f=100	0.69h_b=240	**0.20b_f=35**
ERC-3	HW300×300×10×15	HN350×175×7×11	-270×750×12	-129×270×12	0.57b_f=100	0.69h_b=240	**0.22b_f=38**
ERC-4	HW300×300×10×15	HN350×175×7×11	-270×750×14	-129×270×12	0.57b_f=100	0.69h_b=240	**0.23b_f=40**
ERC-5	HW300×300×10×15	HN350×175×7×11	-270×750×16	-129×270×12	0.57b_f=100	0.69h_b=240	**0.25b_f=43**
ERC-6	HW300×300×10×15	HN350×175×7×11	-270×750×16	-129×270×12	0.57b_f=100	0.69h_b=240	**0.27b_f=48**
IRA-1	HW350×350×12×19	HN350×175×7×11	-312×750×16	-153×312×12	**0.40b_f=70**	0.69h_b=240	0.23b_t=40
IRA-2	HW350×350×12×19	HN350×175×7×11	-312×750×16	-153×312×12	**0.49b_f=85**	0.69h_b=240	0.23b_f=40
IRA-3	HW350×350×12×19	HN350×175×7×11	-312×750×16	-153×312×12	**0.51b_f=90**	0.69h_b=240	0.23b_f=40
IRA-4	HW350×350×12×19	HN350×175×7×11	-312×750×16	-153×312×12	**0.54b_f=95**	0.69h_b=240	0.23b_f=40
IRA-5	HW350×350×12×19	HN350×175×7×11	-312×750×16	-153×312×12	**0.57b_f=100**	0.69h_b=240	0.23b_f=40
IRA-6	HW350×350×12×19	HN350×175×7×11	-312×750×16	-153×312×12	**0.66b_f=115**	0.69h_b=240	0.23b_f=40
IRA-7	HW350×350×12×19	HN350×175×7×11	-312×750×16	-153×312×12	**0.74b_f=130**	0.69h_b=240	0.23b_f=40
IRA-8	HW350×350×12×19	HN350×175×7×11	-312×750×16	-153×312×12	**0.80b_f=140**	0.69h_b=240	0.23b_f=40
IRA-9	HW350×350×12×19	HN350×175×7×11	-312×750×16	-153×312×12	**0.83b_f=145**	0.69h_b=240	0.23b_f=40
IRB-1	HW350×350×12×19	HN350×175×7×11	-312×750×16	-153×312×12	0.57b_f=100	**0.57h_b=200**	0.23b_f=40
IRB-2	HW350×350×12×19	HN350×175×7×11	-312×750×16	-153×312×12	0.57b_f=100	**0.60h_b=210**	0.23b_f=40
IRB-3	HW350×350×12×19	HN350×175×7×11	-312×750×16	-153×312×12	0.57b_f=100	**0.63h_b=220**	0.23b_f=40
IRB-4	HW350×350×12×19	HN350×175×7×11	-312×750×16	-153×312×12	0.57b_f=100	**0.69h_b=240**	0.23b_f=40
IRB-5	HW350×350×12×19	HN350×175×7×11	-312×750×16	-153×312×12	0.57b_f=100	**0.74h_b=260**	0.23b_f=40
IRB-6	HW350×350×12×19	HN350×175×7×11	-312×750×16	-153×312×12	0.57b_f=100	**0.80h_b=280**	0.23b_f=40
IRB-7	HW350×350×12×19	HN350×175×7×11	-312×750×16	-153×312×12	0.57b_f=100	**0.86h_b=300**	0.23b_f=40
IRB-8	HW350×350×12×19	HN350×175×7×11	-312×750×16	-153×312×12	0.57b_f=100	**0.90h_b=315**	0.23b_f=40
IRB-9	HW350×350×12×19	HN350×175×7×11	-312×750×16	-153×312×12	0.57b_f=100	**0.94h_b=330**	0.23b_f=40
IRC-1	HW350×350×12×19	HN350×175×7×11	-312×750×16	-153×312×12	0.57b_f=100	0.69h_b=240	**0.14b_f=25**
IRC-2	HW350×350×12×19	HN350×175×7×11	-312×750×16	-153×312×12	0.57b_f=100	0.69h_b=240	**0.17b_f=30**
IRC-3	HW350×350×12×19	HN350×175×7×11	-312×750×16	-153×312×12	0.57b_f=100	0.69h_b=240	**0.20b_f=35**
IRC-4	HW350×350×12×19	HN350×175×7×11	-312×750×16	-153×312×12	0.57b_f=100	0.69h_b=240	**0.23b_f=40**
IRC-5	HW350×350×12×19	HN350×175×7×11	-312×750×16	-153×312×12	0.57b_f=100	0.69h_b=240	**0.26b_f=45**
IRC-6	HW350×350×12×19	HN350×175×7×11	-312×750×16	-153×312×12	0.57b_f=100	0.69h_b=240	**0.29b_f=50**
EST-1	HW300×300×10×15	HN350×175×7×11	**-270×750×16**	-129×270×12	0.57b_f=100	0.69h_b=240	0.23b_f=40
EST-2	HW300×300×10×15	HN350×175×7×11	**-270×750×14**	-129×270×12	0.57b_f=100	0.69h_b=240	0.23b_f=40
EST-3	HW300×300×10×15	HN350×175×7×11	**-270×750×12**	-129×270×12	0.57b_f=100	0.69h_b=240	0.23b_f=40
EST-4	HW300×300×10×15	HN350×175×7×11	**-270×750×10**	-129×270×12	0.57b_f=100	0.69h_b=240	0.23b_f=40
IST-1	HW350×350×12×19	HN350×175×7×11	**-312×750×14**	-153×312×12	0.57b_f=100	0.69h_b=240	0.23b_f=40
IST-2	HW350×350×12×19	HN350×175×7×11	**-312×750×16**	-153×312×12	0.57b_f=100	0.69h_b=240	0.23b_f=40
IST-3	HW350×350×12×19	HN350×175×7×11	**-312×750×18**	-153×312×12	0.57b_f=100	0.69h_b=240	0.23b_f=40
ESM-1	HW300×300×10×15	HN350×175×7×11	**-270×750×16**	-129×270×12	0.57b_f=100	0.69h_b=240	0.23b_f=40
ESM-2	HW300×300×10×15	HN350×175×7×11	**-270×750×14**	-129×270×12	0.57b_f=100	0.69h_b=240	0.23b_f=40
ESM-3	HW300×300×10×15	HN350×175×7×11	**-270×750×12**	-129×270×12	0.57b_f=100	0.69h_b=240	0.23b_f=40